

The XMM-LSS Survey

First high redshift galaxy clusters: relaxed and collapsing systems^{*}

I. Valtchanov^{1,2}, M. Pierre¹, J. Willis^{3**}, S. Dos Santos¹, L. Jones⁴, S. Andreon⁵, C. Adami⁶, B. Altieri⁷,
M. Bolzonella⁸, M. Bremer⁹, P.-A. Duc¹, E. Gosset¹⁰, C. Jean¹⁰, and J. Surdej¹⁰

¹ CEA/Saclay, Service d'Astrophysique, F-91191, Gif-sur-Yvette, France

² Astrophysics Group, Blackett Laboratory, Imperial College, London SW7 2BW, UK

³ ESO, Ave. Alonso de Cordova 3107, Casilla 19, Santiago 19001, Chile

⁴ School of Physics and Astronomy, University of Birmingham, Birmingham, UK

⁵ INAF-Osservatorio Astronomico di Brera, via Brera 28, 20121 Milano, Italy

⁶ LAM, Traverse du Siphon, 13012 Marseille, France

⁷ ESA, Villafranca del Castillo, Spain

⁸ Istituto di Astrofisica Spaziale e Fisica Cosmica, Sezione di Milano, via Bassini 15, 20133 Milano

⁹ Department of Physics, University of Bristol, H.H. Wills Laboratory, Bristol, UK

¹⁰ Université de Liège, Allée du 6 Août, 17, B5C, 4000 Sart Tilman, Belgium

Received, October 29, 2018, Accepted, October 29, 2018

Abstract. We present five newly found galaxy clusters at $z > 0.6$ from the XMM Large-Scale Structure Survey (XMM-LSS). All five objects are extended X-ray sources in the XMM images. For three of them we have sufficient spectroscopically confirmed member galaxies that an estimate of the velocity dispersion is possible: XLSSC 001 at $z = 0.613$ and $\sigma_V = 867^{+80}_{-60}$ km s⁻¹, XLSSC 002 at $z = 0.772$ and $\sigma_V = 524^{+267}_{-116}$ km s⁻¹ and XLSSC 003 at $z = 0.839$ and $\sigma_V = 780^{+137}_{-75}$ km s⁻¹. These three clusters have X-ray bolometric luminosities $L_X \sim 1 - 3 \times 10^{44}$ erg s⁻¹ and temperatures 2 – 4 keV, and consequently are less massive than previously known clusters at similar redshifts, but nevertheless they follow the low redshift scaling relations between L_X , T and σ_V , within the limits of the measurement errors. One of the clusters, XLSSC 004, is detected independently as an overdensity of galaxies of a colour $R-z'=1.4$ that matches the redshift of the central galaxy $z = 0.87$, although it cannot unambiguously be confirmed by the spectroscopic observations alone. The highest redshift candidate cluster pertaining to this paper, XLSSC 005, is most likely a double cluster complex at a redshift around unity, associated with an extended X-ray source with probable substructure.

Key words. X-rays: galaxies: clusters; Cosmology: large-scale structure of Universe; Surveys

1. Introduction

Statistical samples of distant galaxy clusters can serve as a powerful tool to study the large-scale structure of the Universe. To obtain cluster samples deep enough and over a large area with optical or near-infrared observations is quite a difficult task (e.g. Gunn et al. 1986, Postman et al. 1996, Gonzales et al. 2001, Stanford et al. 1997, Dickinson 1997). Projection effects and the small field-of-view of the current NIR imagers interplay to make relatively large contiguous surveys of distant clusters a dubious game.

Send offprint requests to: Ivan Valtchanov,
e-mail: i.valtchanov@imperial.ac.uk

^{*} Based on observations obtained with XMM-Newton, CFHT, ESO (program ID: 70.A-0283)

^{**} Present address: Dept. of Physics and Astronomy, Univ. of Victoria, Victoria, Canada

On the other hand, a much more efficient strategy is to perform cluster searches in X-rays: galaxy clusters are one of the most powerful X-ray emitting objects, their X-ray emission is of thermal origin (free-free emission of the electrons from the gas trapped into the deep gravitational potential well of the cluster and, in general, in hydrostatic equilibrium) and depends on the square of the gas density and so projection effects are not very important. Another advantage is the fact that high galactic latitude fields of the X-ray sky are populated mostly by two distinct kinds of object: AGNs or QSOs, which appear as point-like, and galaxy clusters, which are extended. It is straightforward to distinguish between the two classes using X-ray telescopes with good spatial and spectral resolution. Namely, galaxy clusters are extended sources radiating by thermal bremsstrahlung with spectra declining steeply with energy and so (depending on the temperature) the major part of the cluster emission is in the soft X-ray band (below 2 keV). On the

other hand, AGNs/QSOs are point-like sources and generally have harder power-law spectra. The spectral distinction, however requires sufficient photon statistics and is prone to many assumptions and uncertainties.

Ever since the first imaging X-ray observations, galaxy clusters were one of the main targets. This has led to flourishing X-ray based cluster surveys, initiated by the Einstein Medium Sensitivity Survey (Gioia et al. 1990) and then continued with ROSAT both at low redshifts (e.g. Ebeling et al. 1998, 2000; De Grandi et al. 1999; Böhringer et al. 1998) and high redshifts (e.g. Rosati et al. 1998, Jones et al. 1998, Romer et al. 2000, Ebeling et al. 2001, Gioia et al. 2001, Burke et al. 2003, Mullis et al. 2003; for a review see Rosati et al. 2002). From these cluster surveys we have gained knowledge about individual objects, scaling relations, studies of the physics of the intra-cluster medium, the large-scale distribution, the clustering properties and the evolution of galaxy clusters.

Nowadays cluster searches and surveys are brought to a new level with Chandra and XMM. Some of these projects are a natural continuation of existing surveys from the previous X-ray missions, following-up interesting objects and to get better insights on cluster physics, while other surveys use the publicly available archives of XMM and Chandra X-ray observations – this is really an inexpensive way to get statistically significant number of serendipitously detected clusters at all redshifts (e.g. Romer et al. 2001, Schwobe et al. 2003, Kim et al. 2004).

The increased sensitivity of XMM and Chandra X-ray observatories, however, can also be exploited to survey large contiguous areas of the sky with relatively short exposure times. A fainter cluster/group population at intermediate redshifts that was not accessible to the previous X-ray missions will thus be detected. In return, this will give us a unique view of the cosmic web at the mass scale traced by this population.

This is the approach of the XMM Large-Scale Structure Survey (XMM-LSS, Pierre et al. 2001a, 2001b). The final objective is to map a contiguous region of the sky and to study the large-scale distribution and the clustering properties of the matter traced by the galaxy clusters and the QSO/AGN population. XMM-LSS is based on XMM observations and a subsequent multi-wavelength follow-up programme. The target XMM-LSS survey geometry and depth were chosen such that to have a statistically significant number of clusters so that the two-point correlation function of clusters at $0 < z < 0.5$ and $0.5 < z < 1$ can be calculated with a precision reaching that of the ROSAT-ESO Flux Limited X-ray Survey (REFLEX, Collins et al. 2000) which covers a much larger area but only goes out to $z < 0.2$.

To achieve this goal we need a good X-ray cluster detection procedure. Using extensive XMM image simulations we have developed an efficient pipeline procedure that uses the full XMM instrument sensitivity and indeed allows us to detect extended sources down to flux levels of 5×10^{-15} erg s⁻¹ cm⁻² for 10 ks exposures (Valtchanov et al. 2001, Refregier et al. 2002). The successful detection is quite crucial because even the mere counting of clusters at different redshifts can be used to constrain cosmological parameters (e.g. Mathiesen & Evrard 1998, Henry 2000, Borgani et al. 2001, Refregier et al. 2002). These cosmological constraints that come from cluster abun-

dance evolution are complementary and independent to those from cosmic microwave background and supernovae studies.

Each detected candidate cluster from the pipeline, depending on its estimated redshift by photometric redshifts, is programmed to a spectroscopic follow-up ($z < 1$) or NIR observations ($z > 1$). The spectroscopic follow-up of the first sample of candidate clusters in the XMM-LSS at $z < 1$ was programmed for observations on Las Campanas/Magellan and on the ESO/VLT telescopes. The subject of this paper is to present the first results for a sample of 5 clusters at $z > 0.6$ while the low redshift sample is presented elsewhere (Willis et al., in preparation).

The paper is organised as follows: first we present the X-ray data reduction and source detection (Sect. 2), then we describe in Sect. 3 the optical identification, spectroscopic target selection procedure and the observations. In Sect. 4, we present the data analysis results from the spectroscopic and X-ray observations. Next we discuss each individual object (Sect. 5) and we end up with the conclusions (Sect. 6). Except where is mentioned, we use Λ CDM cosmology ($H_0 = 70$ km s⁻¹ Mpc⁻¹, $\Omega_m = 0.3$, $\Omega_\Lambda = 0.7$) for all cosmologically dependent parameters. All X-ray luminosities are bolometric.

2. X-ray data

The candidate clusters for the first spectroscopic run were chosen from all XMM-LSS pointings received by August 2002. This includes 15 AO-1 pointings of 10 ks exposure and another 15 exposures of 20 ks from the Guaranteed Time XMM Medium Deep Survey (XMDS). All observations were of good quality, except two fields that suffered from high background contamination affecting more than 50% of the exposure time.

2.1. Data reduction

A detailed description of the pipeline used in the XMM-LSS data reduction will be presented elsewhere (Pacaud et al., in preparation). Here we just briefly mention the main steps. The raw X-ray observations (ODFs) are reduced by the standard XMM Science Analysis System (XMM-SAS) tasks `emchain` and `epchain` for MOS and PN detectors respectively. High background periods, related to soft protons, are excluded from the event lists and raw photon images with a given pixel scale (2.5"/pixel in this case) in different energy bands are then created. Subsequently the raw images for each instrument are filtered using “à trous” (with holes) iterative wavelet technique with a Poisson noise model and a threshold of 10^{-4} (equivalent to 3.7σ in the Gaussian case) for the significant wavelet coefficients (Starck & Pierre 1998, Starck et al. 1998). Each filtered image is then exposure corrected and a mask map that includes bad pixels, CCD gaps and non-exposed CCD regions (generally parts outside the field-of-view of the telescope) are created. Wavelet-filtered, exposure-corrected images for each instrument in a given energy band are added together to form a compound (MOS1+MOS2+PN) single band image to be used in the first stage of the detection procedure.

2.2. Source detection

Clusters of galaxies are extended sources in X-ray images. Their detection and correct classification is not trivial because of various peculiarities of the X-ray observations: Poisson noise regime, varying PSF as a function of the off-axis angle and the energy, the vignetting effect, and the geometry of the detector (CCD gaps). We use images in the [0.5-2] keV energy band which is well suited for clusters and groups (Scharf 2002). The detection procedure is based on the prescription of Valtchanov et al. (2001) and has three stages: wavelet filtering (see the previous section), detection and measurements. The wavelet filtered image is fed to **SExtractor** (Bertin & Arnouts 1996) for detection and characterisation. The classification to extended (clusters) and point-like sources (AGNs or QSOs) is done by using three parameters: the half-light radius, the FWHM from a Gaussian fit to the source and **SExtractor** stellarity index adapted for the X-ray observations. The classification task is complicated by the fact that distant and faint clusters are not too different from a PSF. Moreover, at greater off-axis angles the PSF shape can be quite distorted, although the half-energy width does not change significantly in the [0.5 – 2] keV energy band. This shape distortion can lead to a wrong classification and that is why we have constrained the cluster detection up to off-axis distances not greater than 12'. This strategy gives very good results using simulated XMM images and can be used for selecting cluster candidates with an excellent success rate (Valtchanov et al. 2001).

In total, from the first 3.5 deg² (30 XMM pointings) of XMM-LSS observations, we find some 55 X-ray cluster candidates, which corresponds to ~ 15 clusters per sq.deg., in good agreement with the cosmological predictions (see e.g. Refregier et al. 2002).

3. Optical data

3.1. Optical imaging

Deep images from the CFH12k camera on the Canada-France-Hawaii Telescope (CFHT) in BVRI from the VIRMOS-VLT Deep Survey (VVDS: Le Fèvre et al. 2001, McCracken et al. 2003) were used for optical identifications. The observations were processed by the Terapix team¹ to produce astrometrically and photometrically calibrated images and to create object catalogs by means of **SExtractor**. The definition and magnitude limits of the VVDS may be found in the web pages of the VIRMOS consortium². The X-ray cluster candidates were assigned to *NEAR* ($z < 0.5$) and *MID* ($0.5 < z < 1$) samples by visual inspection of the optical images and also using photometric redshift estimates. We assign all the confident extended sources, that have no obvious optical counterpart in the VVDS images, in the *DIST* ($z > 1$) class for subsequent NIR follow-up. The visual scan of the data was also indispensable for removal of spurious extended sources introduced by instrumental effects. In addition to the CFH12k data, we obtained observations at the CTIO 4m telescope in R and z' which allowed us to

search for a red sequence of galaxies at a given X-ray position (Andreon et al. 2004).

3.2. Spectroscopic target selection

Our driving objective was to confirm the clusters and to measure their redshifts. We chose the ESO-VLT/FORS2 instrument in MXU multi-object spectroscopy mode because of the liberty to place large number of slits with different sizes and orientations and so to optimise the target selection, especially in regions of high galaxy density. Using *fims* (the FORS Instrumental Mask Simulator tool), we placed about 30 slits on average in each mask, possibly placing inclined and longer ones. With the remaining available slits we randomly sampled the X-ray point-like population presented in the same area or just filled the mask with objects from the field, when there were no colour selected or X-ray objects.

We have developed a visualisation procedure to facilitate the selection of spectroscopic targets, optimising the chances to pick up cluster member galaxies. It uses all the available information in the field, combining optical (one band or pseudo-colour VRI image) and X-ray images, colour-magnitude and colour-colour diagrams, and photometric redshift peaks with the corresponding probabilities. In this “multi-parametric space”, first we have taken the objects above the photometric limit, imposed by exposure time and observational strategy constraints. Secondly, we have looked for objects with a plausible colour (V–I or R–I) for ellipticals at the estimated photometric redshift and also used the pseudo-colour images for all candidates for which we have V, R and I observations. The utility of colour information is justified as, out to redshift of unity, the major population of cluster cores is made of ellipticals with an old stellar population (e.g. Dressler et al. 1997, Postman et al. 1998). Moreover, cluster ellipticals at high redshift show-up as an overdensity of red objects in VRI composite images, proving useful in the target selection process. Examples of RGB images for some of the candidate clusters can be found in the web pages of the XMM-LSS consortium³.

3.3. Spectroscopic observations

The ESO-VLT/FORS2 spectroscopic observations in MXU mode were performed on 9-12 October 2002. For the 3 allocated nights in “visitor” mode we selected some 12 candidates from the *NEAR* and *MID* samples. *NEAR* clusters were included in order to provide targets in case of a poor weather and will be presented elsewhere (Willis et al., in preparation). The observing log and object designations for the five *MID* clusters pertaining to this paper are shown in Table 1.

We have used the holographic grism 600RI+19 with the GG435 blocking filter that gives a good response from about 6000 to 8500 Å and a dispersion of 1.64 Å/pixel with the standard instrument resolution. The spectral resolution for slits of 1.4" width as measured from the arc or sky lines was ≈ 6 Å FWHM. The high resolution of the grism ($\lambda/\Delta\lambda = 1000$) makes subsequent sky subtraction easier.

¹ <http://terapix.iap.fr>

² <http://www.astrsp-mrs.fr/virmos/vvds.htm>

³ <http://vela.astro.ulg.ac.be/themes/spatial/xmm/LSS>

Table 1. ESO-VLT observing log. The exposure time is the number of masks times the time, and each mask is split into two exposures.

ID ^a	Cluster	Seeing arcsec	Exposure min.
	09-Oct-2002		
001	XLSS J022457.1–034853	1.0-1.2	2x60
005	XLSS J022709.7–041805	0.7-1.1	2x90
	10-Oct-2002		
004	XLSS J022530.2–050713	0.8-2.7	90+60
	10-Oct-2002		
002	XLSS J022532.5–035510	0.7-1.2	2x60
003	XLSS J022738.2–031757	0.7-1.1	2x60

^a - In the following, all clusters are referred to via the reference XLSSC plus the identification number, e.g. XLSSC 001, etc.

For each mask we split the total observing time into two exposures in order to remove cosmic ray contaminations. We have used the IRAF task `imcombine` with the `crreject` algorithm – appropriate for rejecting cosmic ray events even with two images. The spectral reduction was performed using the standard tools from IRAF: zero level exposure, flat-fielding, cosmic ray removal, aperture selection and sky subtraction using the `apextract` package. For wavelength calibration, we have used He-Ne-Ar lamp exposures observed at the end of the corresponding night. The wavelength calibration was performed with a Chebyshev polynomial of 3rd degree and the residuals were kept inside $\pm 1.0 \text{ \AA}$ with an rms scatter $\sim 0.3 - 0.5 \text{ \AA}$. A standard star was observed in the beginning and at the end of each night with the same instrumental configuration in order to remove the instrumental response and therefore to transform the spectra to relative flux units.

4. Results

4.1. Redshifts

The sky subtracted, wavelength and flux calibrated spectra were used to derive the redshifts. First we obtained a redshift estimate based on the CaII H+K doublet, when present, and then we used the cross-correlation technique as implemented in the RVSAO package (Kurtz & Mink 1998) using an elliptical galaxy template spectrum (Kinney et al. 1996). To improve the cross-correlation signal, we have masked the wavelength ranges of the strongest sky lines, where residuals from the sky subtraction could occur, and also the region of a strong atmospheric absorption at 7750-7800 \AA .

The redshift distributions in each field are shown in Fig. 1. To illustrate the redshift space overdensities we have applied an adaptive kernel smoothing over the redshifts (e.g. Silverman 1986, Pisani 1993). There is both a clear redshift grouping and a spatial grouping associated with the X-ray emission in XLSSC 001, XLSSC 002 and XLSSC 003. For these three cases only we show zoomed in an inset a redshift histogram of the overdensity with a fixed bin size. The derived mean redshift and the velocity dispersion, by means of bi-weighted estimators of location and scale (Beers et al. 1990), are shown

Table 2. Spectroscopic redshift measurements. N_{gal} shows the total number of galaxies used to derive the cluster redshift. The number in parenthesis shows the number of galaxies with [OII] 3727 \AA emission line. See the text for details on XLSSC 004 and XLSSC 005 redshifts.

Name	Redshift	σ_v km/s	N_{gal}
XLSSC 001	$0.6128^{+0.0006}_{-0.0006}$	867^{+80}_{-60}	29(9)
XLSSC 002*	$0.7722^{+0.0001}_{-0.0003}$	524^{+267}_{-116}	11(5)
XLSSC 003	$0.8387^{+0.0007}_{-0.0007}$	780^{+137}_{-75}	17(5)
XLSSC 004	~ 0.87	—	4(1)
XLSSC 005	~ 1.0	—	7(5)

(*) – taking only the objects having redshifts in [0.76, 0.78].

in Table 2; the quoted errors are 1σ bias-accelerated bootstrap errors (Efron & Tibshirani 1986).

For XLSSC 004 and XLSSC 005, the peaks in the redshift distribution over the whole FORS field do not correspond to any significant spatial clustering, and no peak can be unambiguously associated with the extended X-ray source. Nevertheless, we show in Table 2 the most plausible redshift based on measurements of galaxies spatially coincident with the cluster X-ray emission (see Figs. 7 and 8).

4.2. X-ray analysis

Deriving detailed cluster physical characteristics from the X-ray observations is not the main objective of XMM-LSS. Indeed, with exposure times of the order of 10 ks only a small fraction of clusters are expected to have enough photon statistics to allow reliable measurements of the mean temperature, or to distinguish possible AGN contamination. Nevertheless, we have derived the temperature and luminosity for the clusters pertaining to this paper and, in some cases, these parameters were well constrained. These results however must be taken with caution as in some cases possible AGN contamination cannot be ruled out.

For each cluster an X-ray spectrum was extracted from a region large enough to include the cluster emission. A background spectrum was taken from an adjacent annulus. We removed in advance the contribution of all other sources within the cluster and background regions. A photon redistribution matrix (RMF) and ancillary region file (ARF) were created using `XMMSAS:rmfgen/arfggen`, including corrections for bad pixels and detector geometry. Finally the spectra from the three instruments MOS1, MOS2 and PN were regrouped to have at least 25 counts per bin. The extracted spectra were used to derive the observed characteristics shown in Table 3 without any recourse to a reference model.

To get the global cluster X-ray characteristics, the binned spectra in each instrument were fitted to a `mekal` model of thermal plasma emission with photo-electric absorption us-

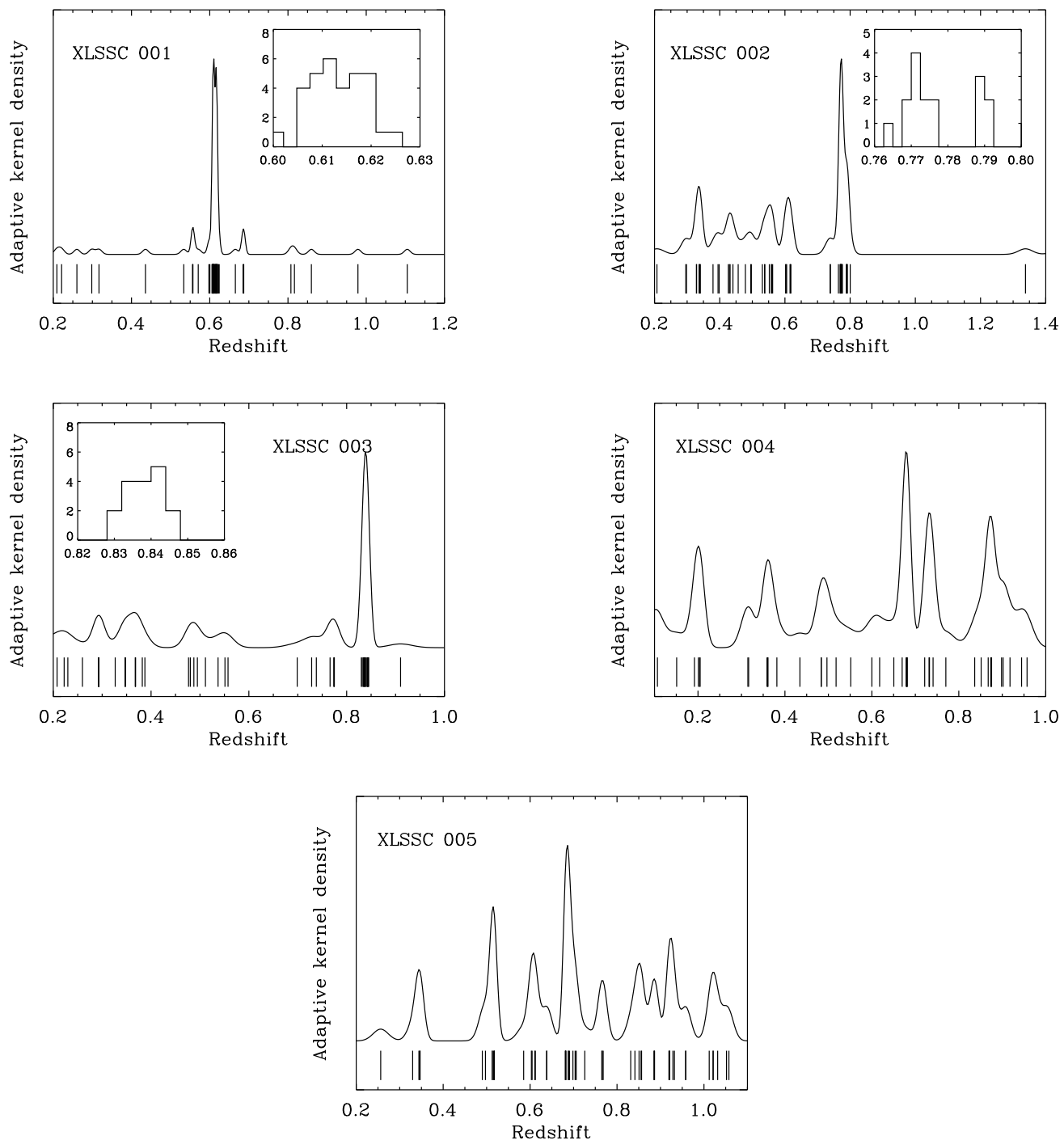


Fig. 1. Redshift distributions of the spectroscopically observed objects for all five clusters. The adaptive kernel density estimation (Silverman 1986) is shown as a continuous line over the redshift measurements. In cases where an overdensity in redshift space corresponds to a spatial correlation we show a histogram of the zoomed redshift region: for XLSSC 001 from 0.6 to 0.63, bin size 0.0027; XLSSC 002: $0.76 < z < 0.80$, bin size 0.0025; XLSSC 003: $0.82 < z < 0.86$, bin size 0.004.

ing XSPEC (Arnaud 1996, also see the XSPEC manual⁴ for the mekal model and corresponding references). The energy range used in the fit is [0.3 – 10] keV for MOS instruments, but for PN we used [0.3 – 7.5] keV in order to avoid an instrumental

emission feature at 8 – 9 keV. We have kept only two free parameters in the fitting: the temperature and the normalisation. The mean Galactic absorption of $N_H = 2.5 \times 10^{20} \text{ cm}^{-2}$ (Dickey & Lockman 1990), the metal abundance of $Z = 0.3Z_\odot$ and the redshift were fixed. For parameter estimation, we used the Cash statistic, modified to allow background subtraction (see

⁴ <http://heasarc.gsfc.nasa.gov/docs/xanadu/xspec/manual/>

Table 3. X-ray parameters. “Region” is the extraction radius in arcmin and in comoving Mpc in brackets. “ R_{50} ” is the object’s half-light radius in arcsec in the [0.5–2] keV band, note that the PSF half-light radius at 10’ off-axis and at 1 keV is 9”. The “Exposure” is the average of the weighted live time events in the extraction region.

Name	Redshift	Region	R_{50}	off-axis	Counts	Exposure
		arcmin(Mpc)	arcsec	arcmin	[0.2–10] keV ALL(MOS1+MOS2+PN)	MOS1+MOS2+PN ks
XLSSC 001	0.6128	1.7(0.78)	32.2	5.8	1812(472+467+873)	2x13.3+7.9
XLSSC 002	0.7722	1.1(0.60)	16.6	9.9	633(177+152+304)	2x13.3+7.9
XLSSC 003	0.8378	1.1(0.65)	23.6	6.0	575(136+128+311)	2x11.5+8.3
XLSSC 004	0.87	0.5(0.27)	—	3.8	233(40+83+110)	2x20.8+16.6
XLSSC 005	1.0	0.83(0.56)	21.1	8.5	353(50+76+227)	24.5+24.9+21.5

the XSPEC manual). The results are shown in Table 4. The errors on the temperature are 1σ , the errors for the flux F_X and the luminosity L_X were calculated varying the normalisation parameter in its 1σ confidence interval, while the temperature was kept fixed at its best fit value. The bolometric X-ray luminosity L_X was calculated using the energy range [0.01–30] keV, constrained only by the instrument response matrices (generally from ~ 0.05 to ~ 20 keV rest frame).

For XLSSC 004 and XLSSC 005 photon statistics are insufficient to allow any plausible parameter estimation so we have estimated the flux and the luminosity by fixing the temperature at 4 keV. The uncertainties in this case came from varying only the normalisation and thus can be quite underestimated.

The cluster masses were estimated from the local $L_X - M$ relation (Reiprich & Böhringer 2002) assuming no evolution. The errors on the mass, reported in Table 4, only reflect the uncertainty on the luminosities and so are significantly underestimated, given the large (up to an order of magnitude!) scatter in the local $L_X - M$ relation.

The X-ray spectra, mekal fit and the corresponding residuals for XLSSC 001, XLSSC 002 and XLSSC 003 are shown in Fig. 2 and the derived model characteristics are given in Table 4.

4.3. Scaling relations

The scalings between the bolometric luminosity, temperature and velocity dispersion from the clusters in the compilation of Wu et al. (1999) are shown in Fig. 3, together with the objects pertaining to this paper. XLSSC 001, XLSSC 002 and XLSSC 003 are in good agreement with the scaling relations $L_X - \sigma_v$, $L_X - T$ and $\sigma_v - T$ (Xue & Wu 2000, Arnaud & Evrard 1999), although caution must be taken because of possible biases on the temperature introduced by the insufficient photon statistics (see e.g. Fairley et al. 2000). What is important to note is that the three clusters are at lower temperatures and luminosities than the other known clusters at high redshift. In that sense we are starting to reach moderately massive systems at high redshift, whilst from ROSAT or EINSTEIN surveys the distant clusters are rather more luminous and consequently more massive systems.

Table 4. Derived, model dependent, cluster X-ray characteristics. The data presented for XLSSC 004 and XLSSC 005 is for fixed temperature of 4 keV and the uncertainties are probably underestimated. The reported masses should be treated with extreme caution as the scatter in the local $L_X - M$ relation is large. See text for details.

Name	Redshift	kT keV	F_X^a	L_X^b	M^c
XLSSC 001	0.6128	$3.4^{+1.1}_{-0.8}$	$8.9^{+1.0}_{-0.7}$	$3.5^{+0.3}_{-0.3}$	$4.4^{+0.2}_{-0.2}$
XLSSC 002	0.7722	$2.2^{+1.3}_{-0.6}$	$2.6^{+0.7}_{-0.4}$	$1.7^{+0.4}_{-0.3}$	$2.9^{+0.5}_{-0.5}$
XLSSC 003	0.8378	$4.1^{+4.7}_{-1.8}$	$4.4^{+1.0}_{-0.8}$	$3.7^{+0.9}_{-0.6}$	$4.3^{+0.5}_{-0.4}$
XLSSC 004	0.87	4	$0.23^{+0.2}_{-0.2}$	$0.21^{+0.1}_{-0.1}$	$0.8^{+0.9}_{-0.9}$
XLSSC 005	1.0	4	$1.03^{+0.3}_{-0.2}$	$1.32^{+0.3}_{-0.3}$	$2.0^{+0.3}_{-0.3}$

^a – the unabsorbed flux F_X in the [0.5–2] keV band and in units of 10^{-14} erg s^{-1} cm^{-2} .

^b – the luminosity L_X is pseudo-bolometric ([0.01–30] keV) and in units of 10^{44} erg s^{-1} .

^c – the total mass M in units of $10^{14} M_\odot$, based on the local $L_X - M$ relation.

5. Individual objects

The optical/X-ray overlays for all candidates are shown in Figs. 4–8. The optical images are from CFHT/CFH12k camera in the I-band, the X-ray contours are from wavelet filtered MOS1+MOS2+PN images (see Sec. 2). For XLSSC 001, XLSSC 002 and XLSSC 003, the objects from the inset histograms of their redshift distribution (Fig. 1) are denoted as boxes and triangles, the latter for the galaxies with [OII] 3727 Å emission line. When there was no obvious redshift peak (XLSSC 004 and XLSSC 005) we indicate the redshift of each spectroscopically observed galaxy.

Based on the morphology, redshift distribution and the visual appearance, we define three broad cluster classes: relaxed, relaxing and collapsing.

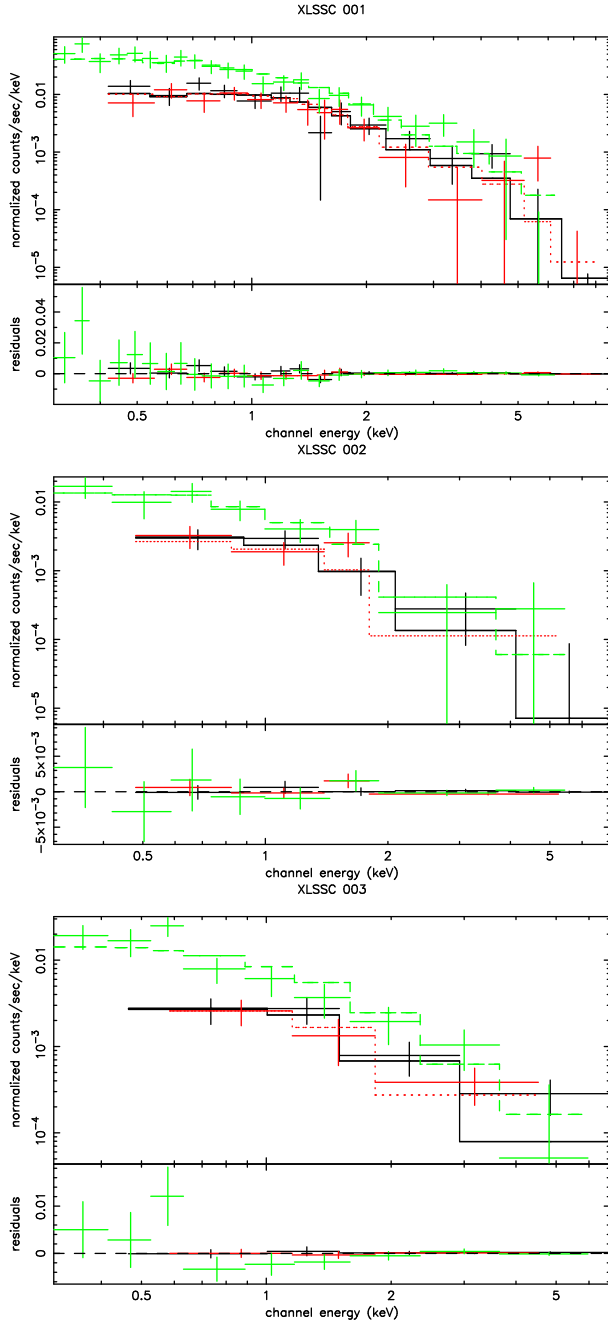


Fig. 2. X-ray spectra, model fit and the corresponding residuals for MOS1 (in black, the continuous histogram shows the model fit), MOS2 (in red, the dotted histogram is the model fit) and PN (in green, the model fit is the dashed histogram). The spectra were initially regrouped to have at least 25 photons per energy bin.

5.1. Relaxed cluster: XLSSC 003

XLSSC 003 (Fig. 6) has the appearance of a relaxed cluster with velocity distribution close to a Gaussian. Normality tests (Anderson-Darling and Shapiro-Wilk, see e.g. D’Agostino & Stephens 1986) accept the null hypothesis of the distribution being drawn from a normal distribution at 90% confidence, but this must be taken with caution as the number of objects is small. The X-ray emission is slightly elongated and there is no

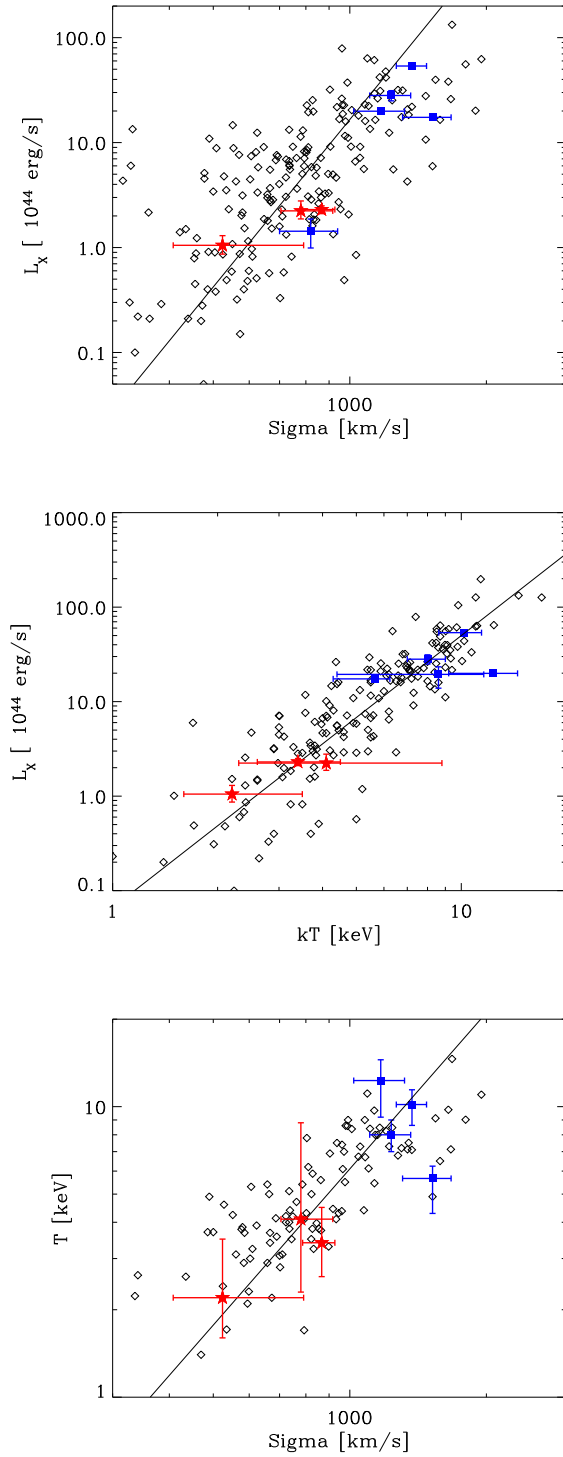


Fig. 3. The scaling relations: luminosity-velocity dispersion ($L_X - \sigma_v$, upper panel), luminosity-temperature ($L_X - T$, middle panel) and velocity dispersion-temperature (lower panel). The clusters from the compilation of Wu et al. (1999) are denoted as diamonds and those at $z \geq 0.5$ are shown as blue boxes with error bars. The best fit from Xue & Wu (2000) for $L_X - \sigma_v$ and $\sigma_v - T$ and from Arnaud & Evrard (1999) for $L_X - T$ are shown as lines. The objects pertaining to this paper are shown as filled red stars with the corresponding error bars. For this comparison only, their luminosity was transformed to Einstein-de Sitter cosmology with $H_0 = 50 \text{ km s}^{-1}$ and $\Lambda = 0$ ($q_0 = 0.5$).

evidence of substructure. The brightest cluster galaxy coincides with the X-ray emission peak and is at rest with respect to the cluster mean ($z_{BCG} = 0.8382$, $\Delta v = 65 \text{ km s}^{-1}$).

As can be seen from Tabs. 3 and 4, the low photon statistics do not allow the temperature to be constrained, although if we assume an equipartition between the galaxy velocities and the gas, i.e. $kT = \mu m_p \sigma_v^2$, we derive a temperature of $kT = 3.9 \pm 1.5 \text{ keV}$ – in excellent agreement with the best fit value.

5.2. Relaxing cluster: XLSSC 001

Morphologically XLSSC 001 (Fig. 4) looks like present day still relaxing clusters: there is an obvious centre formed by the brightest cluster galaxies displaced at $\sim 10''$ from the X-ray emission peak. The brightest cluster galaxy (BCG) has a typical giant elliptical galaxy absorption spectrum and is at 750 km s^{-1} with respect to the mean cluster redshift. The velocity distribution is quite broad, but the null hypothesis that the observed distribution is drawn from normal cannot be ruled out – the Anderson-Darling statistics value is 0.527 which is less than the critical value 0.616 needed to reject the normality assumption at 90% confidence level.

There are two other X-ray sources projected over the cluster emission. One is the subclump to the north-east, which is most likely associated with the cluster as there are three cluster members within the X-ray contours (two of which are emission line galaxies) and no obvious optical counterpart at the X-ray peak. Unfortunately, due to instrumental problems, we could not get the optical spectrum of the south-east point-like source.

The X-ray characteristics of the cluster are relatively well constrained as we have about 1600 photons in the spectrum and the cluster is of low temperature. The low luminosity of the cluster is in agreement with its temperature and the velocity dispersion, as compared to the scaling relations of local clusters (Fig. 3).

5.3. Collapsing cluster: XLSSC 002

XLSSC 002 (Fig. 5) resembles a point-like source in X-rays, although its half-light radius is $R_{50} \approx 17''$ (see Table 3, to be compared to the PSF half-energy radius of $9''$) and the extension log-likelihood (as reported by the XMM-SAS task `emldetect`) is 7.4, corresponding to probability of 6×10^{-4} of being a point-like source. The 8 centrally located galaxies form a crown-like figure, and five are in a very narrow redshift range 0.771 – 0.775 most likely forming a compact core. The brightest cluster galaxy is at redshift coinciding with the mean of the centrally located galaxies ($z_{BCG} = 0.7714$) and has a typical giant elliptical galaxy absorption spectrum.

We have to note that there are galaxies at similar redshifts ($z \approx 0.77$) all over the field as can be seen in Fig. 5. None of the other X-ray sources present in the field are cluster members.

The temperature is quite tightly constrained by the X-ray spectral fit even though the photon statistics seems rather poor – 480 photons in the [0.2-10] keV band in total. This is possible as the cluster is at low temperature. The relations between clus-

ter global characteristics, L_X , T and σ_V (Fig. 3) are consistent with those observed from local clusters.

There is a large fraction of emission-line galaxies in the centre (5 from 8) as identified by the presence of the [OII] 3727 Å line. This line is not broad in Type 1 AGN, and thus it is difficult to assess the presence of an AGN with only this one emission feature – most of the diagnostic line ratios that can be used involve lines (H_β , [OIII] 4959+5007 Å, H_α) outside the range of the grism RI600 used in this spectroscopic run. Optical-to-X-ray flux ratios from deep surveys suggest that AGN with magnitudes typical of these galaxies have X-ray fluxes covering a wide range, between $\approx 8 \times 10^{-16}$ and $\approx 8 \times 10^{-15} \text{ erg cm}^{-2} \text{ s}^{-1}$ (0.5-2 keV), with the mean being $\approx 2 \times 10^{-15} \text{ erg cm}^{-2} \text{ s}^{-1}$ (eg. Mainieri et al. 2002). Even in the unlikely event that all 5 emission line galaxies contain X-ray emitting AGN at this mean flux, the total would only be $\approx 40\%$ of the measured cluster flux. It is perhaps more likely that most are Butcher-Oemler star-forming galaxies, implying an interestingly high star-forming fraction (eg. Fairley et al. 2002 find blue fractions up to 40% in low L_X clusters at $z \sim 0.3$). Pending further studies of the galaxy population, we conclude that some contamination by AGN may be possible, but that it is unlikely that all the X-ray flux originates in AGN.

Based on the morphology and the redshift distribution, the most plausible interpretation is that the cluster is in its early stage of formation: a compact core is already formed and the accretion of matter from the nearby large-scale structure is underway – many galaxies in the field have redshifts around the redshift of the central core.

5.4. Other cases

XLSSC 004: The cluster X-ray emission (see Fig. 7) lies between two bright X-ray sources identified as QSOs at $z = 1.12$ (the closest to the north-west, with 486 counts in the [0.5-5] keV band and $V = 21.2$, $R = 20.9$, $I = 20.8$) and at $z = 1.19$ (to the south-east, with 378 counts and $V = 18.5$, $R = 18.5$, $I = 18.0$). These two QSOs are located in diametrically opposed directions at $0.9'$ and $1.2'$ from the centre of the cluster X-ray emission, respectively. Such a configuration is very unlikely to occur by chance. Our estimated surface density is approximately 30 X-ray sources per deg^2 over a field of 2.8 deg^2 in the XMM-LSS survey with detected counts greater than 300, subsequently the probability of detecting two X-ray sources within $2'$ from the cluster X-ray centre is about 1%. Given that these two quasars are located just behind a putative foreground cluster at $z = 0.9$ (see below), gravitational lensing could possibly affect the real positions and fluxes of these two background objects. However, the hypothesis that these QSOs could be two images of a single source lensed by a foreground cluster does not hold as their optical spectra show a significant redshift difference $\Delta z \approx 0.07$. A more detailed discussion on this unusual association will be presented elsewhere (Jean et al., in preparation).

We cannot confirm the reality of the cluster from the spectroscopic observations only – the brightest galaxy inside the X-ray emission is at $z = 0.868$ and there is another one at $15''$ to

the south-east at a similar redshift, $z = 0.874$. Two more galaxies at north-west are at similar redshift 0.875, although outside the detected X-ray emission.

XLSSC 004 is, however, independently detected on a scale of 1 arcmin diameter (marked as a thick green circle in Fig. 7) as an overdensity of galaxies with a similar colour of $R-z' = 1.4^m$, and cluster optical luminosity function compatible with $z = 0.9$ (Andreon et al. 2004).

The peak in the redshift distribution at $z \approx 0.68$ (see Fig. 1) does not correspond to any spatial grouping.

XLSSC 005: This is a very interesting and complicated case. The morphology of the X-ray emission suggests a bimodality, with a central extended source and a possible subclump to the south-east (see Fig. 8). It is not trivial, however, to disentangle the centre, where galaxies at $z = 0.92 - 0.96$ and $z = 1.02 - 1.06$ are mixed. The redshift space distance is rather significant: $\Delta z \sim 0.1$ ($\sim 15000 \text{ km s}^{-1}$) which rules out the galaxies belonging to one and the same cluster.

This cluster has been observed in the K' band with ESO-NTT/SOFI in the framework of the XMM-LSS VIRMOS Deep Survey over an area of 0.25 deg^2 (Iovino et al. 2004, in preparation). The exposure of 1.5 hours resulted in a catalog down to a limiting magnitude $K'_{AB} \approx 22.7$. A search for overdensities in photometric redshift slices of $\Delta z_{phot} = 0.2$ was made, with z_{phot} calculated from BVRIK' photometry. As a result, there is a strong detection with signal-to-noise (S/N) ~ 5 of an overdensity at $z \approx 0.9$ centred on the south-east extension of the X-ray emission. Observations in K at ESO-NTT/SOFI and R and z' at CTIO (Andreon et al. 2004) also indicate two overdensities of galaxies with colours compatible with $z \approx 1$.

The large fraction of emission line objects is also striking. From 5 objects near the X-ray peak with redshifts between $0.92 - 1.06$, 3 have detectable [OII]3727Å emission in their spectra. As in the case of XLSSC 003, it is difficult to assess the presence of an AGN from this one emission line. At these redshifts, broad [MgII]2800Å would be detectable, but in no case was it found.

Based on the X-ray-to-optical flux ratios it is possible that some contribution to the overall X-ray emission might be due to AGN, but unlikely that all of it is due to AGN.

Our preliminary interpretation is that we are observing two clusters in projection: one at $z \sim 0.93$, forming the main body of the extended X-ray source, and the more distant one at $z = 1.02$, that is partially covered. The redshifts of the spectroscopically observed objects inside the X-ray emission span all of the interval from $z \sim 0.92$ to $z \sim 1.05$. This could be an indication of that some of these galaxies may lie on a filament connecting both clusters. Their number, however, is insufficient for any strong claim.

Note that XLSSC 005 is very similar to the case of RXJ1053.7+5735 (Hasinger et al. 1998) – a double cluster at $z = 1.14$ (Hashimoto et al. 2004), which was repeatedly reported in the literature at $z = 1.26$, mistakenly taken a cD-like galaxy from the background as the cluster central galaxy. Thanks to the deepest XMM single pointing observation it was possible to disentangle RXJ1053.7+5735. Unfortunately we cannot apply the same technique as the exposure time in our case is ~ 50 times shorter. XLSSC 005 is however a good tar-

get for deep integral field spectroscopy observations (e.g. IFU of the VIMOS instrument) that will help us resolve this extremely interesting case.

Fig. 4. XLSSC 001. CFH12k I-band image of a $7' \times 7'$ field is shown. North is up and east to the left. The X-ray contours run from 0.1 to 5 counts/pixel ($2.5''$ pixel size) with 10 levels in log space. Objects in the $0.6 \leq z \leq 0.63$ redshift range are denoted by boxes and triangles (for emission-line objects).

Fig. 5. XLSSC 002. A $7' \times 7'$ field is shown and the objects at $0.76 \leq z \leq 0.81$ are denoted by boxes and triangles (for emission-line objects). The X-ray contours run from 0.1 to 5 photons/pixel with 10 levels in log space, with the lowest cluster contour at 0.1 photons/pixel.

Fig. 6. XLSSC 003. Only the central $5' \times 5'$ region of the field is shown and the objects in $0.82 \leq z \leq 0.86$ are denoted by boxes and triangles (for emission-line objects). The X-ray contours run from 0.1 to 5 photons/pixel with 10 levels in log space, and the lowest cluster contour is at 0.1 photons/pixel.

Fig. 7. XLSSC 004. Only the central $3.4' \times 3.4'$ region of the field is shown and the redshifts for the spectroscopically observed objects at $z > 0.8$ are indicated. The triangles denote emission-line objects. The X-ray contours run from 0.15 to 5 photons/pixel with 10 levels in log space, with the lowest cluster contour at 0.15 photons/pixel. The optical detection from CTIO Rz' data is shown as a green circle.

Fig. 8. XLSSC 005. Only the central $3' \times 3'$ region of the field is shown and the redshifts for the spectroscopically observed objects at $z > 0.2$ are indicated. The triangles denote emission-line objects. The X-ray contours run from 0.15 to 5 photons/pixel with 10 levels in log space, with the lowest cluster contour at 0.15 photons/pixel.

6. Conclusions

We present five newly discovered high redshift, X-ray selected clusters in the XMM Large-Scale Structure Survey. The detection and classification in X-rays, the subsequent optical identification and spectroscopic target selection demonstrate the efficiency of the programme and the associated follow-up.

6.1. Highlights

- The five newly discovered X-ray clusters at $z > 0.6$ were observed at ESO-VLT for 11.5 hours in total. For three of them, we have measured more than 15 galaxies with concordant redshifts and thus obtained a viable estimate of the velocity dispersion.
- Thanks to the optimised target selection, we were able to get an estimate of the velocity dispersion of XLSSC 003 at $z = 0.84$ in a reasonable VLT time of 2 hours. To show the potential of the XMM-LSS it is interesting to note that to date there are 5 known clusters in the literature (two of them are X-ray selected) at $z > 0.8$ with more than 10 spectroscopically measured concordant redshifts.
- We have detected a complex structure at a redshift of unity – XLSSC 005. The X-ray morphology and the presence of galaxy overdensity in photometric redshift space and in K, R and z' colour space allow us to speculate that most likely we see two clusters in projection. Some galaxies included in the spectroscopic observations may reside in a possible filament connecting the two clusters.
- From CTIO R z' observations, XLSSC 004 is detected as an overdensity of R- $z'=1.4^m$ galaxies, matching the redshift $z \sim 0.9$ of two bright and centrally located galaxies inside the X-ray extended emission.
- From Tables 3 and 4, and Fig. 3, it is obvious that for the first time we are unveiling, in a systematic manner, moderate mass clusters in the redshift range $0.5 < z < 1$. Most of these objects are weak, extended X-ray sources and consequently would have been difficult to classify in typical deep ROSAT/PSPC pointings because of the insufficient photon statistics in addition to the worse PSF, although there are successful ROSAT identifications of a handful of clusters at similar redshifts and mass scales (eg. Maughan et al. 2003, Vikhlinin et al. 2002). Thus, with XMM-LSS we are starting to fill the cluster database with significant number of objects at high redshift from the middle of the mass function. This is a great improvement upon ROSAT based cluster surveys and will bring important new information on cosmological constraints as well as on non-gravitational physics in clusters (as the effects like pre-heating and feedback are presumably more important in lower mass systems).

6.2. Prospects

In the near future, our goal will be to confirm, via spectroscopic identifications, all XMM-LSS clusters down to $\sim 8 \times 10^{-15}$ erg s^{-1} cm^{-2} over ~ 8 sq.deg. of the AO-1 and AO-2 observations. This will form a complete sample of about 100 X-ray selected clusters at $0 < z < 1$. A follow-up of the most interesting objects at $z \sim 1$ is also previewed with integral-field spectroscopy and possibly deeper targeted X-ray observations with XMM or Chandra for better insight into the cluster physics.

Acknowledgements. MP and IV are grateful to the ESO/Santiago Office for Science, for a two week stay in October 2002, where the analysis of the VLT data presented here was initiated. We are very thankful for the help by G. Marconi and the ESO/VLT team during

the observing run. SDS is supported by a post-doctoral position from the Centre National d'Etudes Spatiales. We wish to thank the referee, H. Ebeling, for his critical approach that helped to improve the paper.

This research has made use of the X-Rays Clusters Database (BAX) which is operated by the Laboratoire d'Astrophysique de Midi-Pyrénées (LAOMP), under contract with the Centre National d'Etudes Spatiales (CNES) and of the NASA/IPAC Extragalactic Database (NED) which is operated by the Jet Propulsion Laboratory, California Institute of Technology, under contract with the National Aeronautics and Space Administration.

References

- Andreon S. et al. 2004, MNRAS, submitted
- Arnaud K.A. 1996, in ASP Conf. Ser., Vol. 101, Astronomical Data Analysis Software and Systems V, eds. Jacoby G.H. & Barnes J. (San Francisco: ASP), 17 (XSPEC)
- Arnaud K.A. 2001, ApJ, submitted
- Arnaud M. & Evrard A. 1999, MNRAS, 305, 631
- Beers T.C., Flynn K. & Gebhardt K. 1990, AJ 100, 32
- Bertin E. & Arnouts S. 1996, A&AS, 117, 393 (SExtractor)
- Böhringer H., Schueker P., Guzzo L., et al. 2001, A&A, 369, 826
- Borgani S., Rosati P., Tozzi P., et al. 2001, ApJ 561, 13
- Burke D.J., Collins C.A., Sharples R.M., et al. 2003, MNRAS, 341, 1093
- Collins C.A., Guzzo L., Böhringer H., et al. 2000, MNRAS, 319, 939
- D'Agostino R.B. & Stephens M.A. 1986, Goodness-of-fit Techniques (New York: Marcel Dekker)
- Danese L., De Zotti G. & di Tullio G. 1980, A&A, 82, 322
- De Grandi S., Böhringer H., Guzzo L., et al. 1999, ApJ, 514, 148
- Dickey J.M. & Lockman F.J. 1990, ARA&A, 28, 215
- Dickinson M. 1997. in "The Early Universe with the VLT", ed. J. Bergeron. Berlin: Springer
- Dressler A., Oemler A., Couch W., et al. 1997, ApJ, 490, 577
- Ebeling H., Edge A.C., Böhringer H., et al. 1998, MNRAS 301, 881
- Ebeling H., Edge A.C., Allen S.W., et al. 2000, MNRAS, 318, 333.
- Ebeling H., Edge A.C. & Henry J.P. 2001, ApJ, 553, 668
- Efron B. & Tibshirani R. 1986, Stat. Sci., 1, 54
- Fairley B.W., Jones L.R., Scharf C., et al. 2000, MNRAS, 315, 669
- Fairley B.W., Jones L.R., Wake D.A., et al. 2002, MNRAS, 330, 755
- Gioia I.M., Maccacaro T., Schild R.E., et al. 1990, ApJS, 72, 567
- Gioia I.M., Henry J.P., Mullis C.R., et al. 2001, ApJ, 553, 105
- Gladders M.D. & Yee H.K.C. 2000, AJ, 120, 2148
- Gonzalez A.H., Zaritsky D., Dalcanton J.J., & Nelson A.E. 2001, ApJS, 137, 117
- Gunn J.E., Hoessel J.G., & Oke J.B. 1986, ApJ, 306, 30
- Hashimoto Y., Barcons X., Böhringer H., et al. 2004, A&A, 417, 819
- Hasinger G., Burg R., Giacconi R., et al. 1998, A&A, 329, 482
- Henry J.P. 2000, ApJ, 534, 565
- Jones L.R., Scharf C.A., Ebeling H., et al. 1998, ApJ 495, 100
- Kim D.-W., Cameron R.A., Drake J.J., et al. 2004, ApJS, 150, 19
- Kinney A., Calzetti D., Bohlin R., et al. 1996, ApJ, 467, 38
- Kurtz M.J. & Mink D.J. 1998, PASP, 110, 934
- Le Fèvre O., Mellier Y., McCracken H.J., et al. 2001, in "New Era of Wide-Field Astronomy", Eds. R.G. Clowes, A.J. Adamson, G.E. Bromage, ASP conference series, Vol. 232, p449
- Maimieri V., Bergeron J., Hasinger G., et al. 2002 A&A 393, 425
- Mathiesen B. & Evrard A. 1998, MNRAS, 295, 769
- Maughan B.J., Jones L.R., Ebeling H., et al., 2003, ApJ, 587, 589
- McCracken H.J., Radovich M., Bertin E., et al. 2003, A&A, 410, 17
- Mullis C.R., McNamara B.R., Quintana H., et al. 2003, ApJ, 594, 154
- Pierre M., Alloin D., Altieri B., et al. 2001, ESO Messenger, 105, 32

- Pierre M., Valtchanov I. & Refregier A. 2001, in “New Visions of the X-ray Universe in the XMM-Newton and Chandra Era”, eds. F. Jansen et al., ESA SP-488 (astro-ph/0202117)
- Pisani A. 1993, MNRAS, 265, 706
- Postman M., Lubin L.M., Gunn J.E., et al. 1996, AJ, 111, 615
- Postman M., Lubin L. & Oke J. 1998, AJ, 116, 560
- Raymond J.C. & Smith B.W. 1977, ApJS 35, 419
- Refregier A., Valtchanov I. & Pierre M. 2002, A&A, 390, 1
- Reiprich T.H. & Böhringer H. 2002, ApJ, 567, 716
- Romer A.K., Nichol R.C., Holden B.P., et al. 2000, ApJS 126, 209
- Romer A.K., Viana P.T.P., Liddle A.R. & Mann R.G. 2001, ApJ, 547, 594
- Rosati P., Della Ceca R., Norman C. & Giacconi R. 1998, ApJ, 492, L21
- Rosati P., Borgani S. & Norman C. 2002, ARAA, 40, 539
- Scharf C. 2002, ApJ, 572, 157
- Silverman B. 1986, Density Estimation for Data Analysis and Statistics (London: Chapman & Hall)
- Stanford S.A., Elston R., Eisenhardt P.R., et al. 1997, AJ, 114, 2232
- Starck J.-L. & Pierre M. 1998, A&AS 128, 397
- Starck J.-L., Murtagh F. & Bijaoui A. 1998, Image Processing and Data Analysis. The Multiscale Approach. Cambridge University Press
- Schwobe A.D., Lamer G., Burke D. et al. 2003, In Proc. COSPAR World Space Congress, in press (astro-ph/0306112)
- Tonry J.L. & Davis M. 1979, AJ, 43, 393
- Tozzi P., Rosati P., Ettori S., et al. 2003, ApJ, 593, 705
- Valtchanov I., Pierre M. & Gastaud R. 2001, A&A, 370, 689
- Vikhlinin A., Van Speybroeck L., Markevitch M., et al. 2002, ApJ, 578, L107
- Wu X.-P., Xue Y.-J. & Fang L.-Z. 1999, ApJ, 524, 22
- Xue Y.-J. & Wu X.-P. 2000, ApJ, 538, 65

This figure "MS3929f4.jpeg" is available in "jpeg" format from:

<http://arxiv.org/ps/astro-ph/0305192v2>

This figure "MS3929f5.jpeg" is available in "jpeg" format from:

<http://arxiv.org/ps/astro-ph/0305192v2>

This figure "MS3929f6.jpeg" is available in "jpeg" format from:

<http://arxiv.org/ps/astro-ph/0305192v2>

This figure "MS3929f7.jpeg" is available in "jpeg" format from:

<http://arxiv.org/ps/astro-ph/0305192v2>

This figure "MS3929f8.jpeg" is available in "jpeg" format from:

<http://arxiv.org/ps/astro-ph/0305192v2>